REGULAR PAPER

Nicolas Hautière · Jean-Philippe Tarel ·
Jean Lavenant · Didier Aubert

Automatic fog detection and estimation of visibility distance through use of an onboard camera

Abstract In this paper, we will present a technique for measuring visibility distances under foggy weather conditions using a camera mounted onboard a moving vehicle. Our research has focused in particular on the problem of detecting daytime fog and estimating visibility distances; thanks to these efforts, an original method has been developed, tested and patented. The approach consists of dynamically implementing Koschmieder's law. Our method enables computing the meteorological visibility distance, a measure defined by the International Commission on Illumination (CIE) as the distance beyond which a black object of an appropriate dimension is perceived with a contrast of less than 5%. Our proposed solution is an original one, featuring the advantage of utilizing a single camera and necessitating the presence of just the road and sky in the scene. As opposed to other methods that require the explicit extraction of the road, this method offers fewer constraints by virtue of being applicable with no more than the extraction of a homogeneous surface containing a portion of the road and sky within the image. This image preprocessing also serves to identify the level of compatibility of the processed image with the set of Koschmieder's model hypotheses.

N. Hautière (✉) · J.-P. Tarel · J. Lavenant · D. Aubert
LIVIC, a joint INRETS-LCPC entity, 14 route de la Minière, Bldg.
824, 78000 Versailles-Satory, France
E-mail: nicolas.hautiere@lcpc.fr

Present Address:
J.-P. Tarel
LCPC (DESE), 58 Bd Lefebvre, 75732 Paris, Cedex 15, France

J. Lavenant
SETRA (CITS), 46 avenue Aristide Briand BP 100, 92225 Bagneux
Cedex, France

1 Introduction

In the aim of reducing the number of traffic accidents or at least limiting their impact, vehicles are increasingly being fitted with active safety systems. Such systems however only prove effective once the accident is well into its occurrence phase. In order to avoid this type of situation from arising in the first place, it becomes necessary to anticipate the associated risks and act accordingly. This stage requires good perception coupled with an acute understanding of the driving environment. This framework has given rise to introducing special sensors (cameras, laser, radar) into certain vehicles.

These sensors have been designed to operate within a wide range of situations and conditions (weather, luminosity, etc.) with a prescribed set of variation thresholds. Effectively detecting when a given operating threshold has been surpassed constitutes a key parameter in the creation of driving assistance systems that meet required reliability levels. With this context in mind, an atmospheric visibility measurement system may be capable of quantifying the most common operating range of onboard exteroceptive sensors. This information is then utilized to adapt sensor operations and processing or to alert the driver that the onboard assistance system is momentarily inoperative.

Moreover, a system capable of either detecting the presence of fog or estimating visibility distances constitutes in itself a driving aid. During foggy weather, humans actually tend to overestimate visibility distances [1], which can lead to excessive driving speeds. A measurement of available visibility would serve to inform the driver that the vehicle speed is not adapted or could even limit the speed automatically depending on specific momentary conditions.

We have sought to build such a system through use of an onboard camera. The onboard nature of the application however does not allow us from generating, at any point in time, a reference image. Furthermore, by using just a single camera, the depth view of the scene of each image is unknown. Given that we are not actually performing temporal monitoring within the scene, the elements at our disposal for developing the method are restricted, due to the nature of

the application context, to the presence of road and sky in the image.

The solution proposed herein is able to overcome these obstacles to a large extent. A preprocessing procedure, by means of region growing, enables locating the most pertinent objects in the image for subsequent application of the newly developed method. The success of this preprocessing step provides direct information on the level of compatibility between the processed image and the set of Koschmieder's law hypotheses. Our method then makes it possible to recover not only the various parameters of Koschmieder's law, but by the same occasion the visibility distance as well.

We will begin by proposing a modeling approach for fog, along with a state of current knowledge as regards visibility distance measurement methods. We will then turn our attention to modeling the sensor and discussing Koschmieder's law from a new perspective. The paper will follow with a presentation of our image preprocessing technique and the method employed to compute Koschmieder's Law parameters; we will finish by discussing some of the experimental results heretofore obtained.

2 Fog modeling

2.1 Definition

Fog is an accumulation of water droplets or ice crystal fines accompanied by hygroscopic, water-saturated fine particles that act to reduce visibility. Its composition is thus identical to that of a cloud whose base would actually touch the ground. Whenever horizontal visibility has been diminished to less than 1 km, the term fog gets employed. Should the level of visibility reach or surpass this threshold, the appropriate term would be mist.

2.2 Propagation of light through fog

In the presence of fog, visible light (with a wavelength situated between 400 and 700 nm) must be propagated within an aerosol that contains a large number of water droplets. During its trajectory, the light from headlamps is attenuated by the dual phenomena of absorption and diffusion, which leads to characterizing fog by means of an extinction coefficient k (equal to the sum of the absorption and diffusion coefficients). In reality however, the absorption phenomenon is negligible in this type of aerosol. The predominant phenomenon therefore proves to be diffusion, which acts to deviate light rays from their initial direction. Such is the origin of fog illumination, or haze luminance, a phenomenon so highly characteristic of daytime fog. These effects have been described by Dumont in [2]. The general problem of optical imaging through fog has been notably studied by Jaruwatanadilok in [3].

2.3 Koschmieder's model

In 1924, Koschmieder [4] proposed his theory on the apparent luminance of objects observed against background sky on the horizon. In noting that a distant object winds up blending in with the sky, he established a simple relationship between the distance d of an object with the intrinsic luminance L_0 and its apparent luminance L as follows:

$$L = L_0 \, e^{-kd} + L_f(1 - e^{-kd}) \qquad (1)$$

where L_f denotes the luminance of the sky and k the extinction coefficient of the atmosphere.

Based on these results, Duntley [4] derived an attenuation law of atmospheric contrasts:

$$C = C_0 \, e^{-kd} \qquad (2)$$

where C designates the apparent contrast at distance d and C_0 the intrinsic contrast of the object against its background.

This law is only applicable in the case of uniform illumination of the atmosphere. In order for the object to be just barely visible, the value of C must equal the contrast threshold ε. From a practical standpoint, the International Commission on Illumination (CIE) [5] has adopted an average value of $\varepsilon = 0.05$ for the contrast threshold so as to define a conventional distance, called the "meteorological visibility distance" V_{met}, i.e. the greatest distance at which a black object ($C_0 = 1$) of a suitable dimension can be seen in the sky on the horizon.

$$V_{met} = -\frac{1}{k} \ln(0.05) \simeq \frac{3}{k} \qquad (3)$$

3 Current state of knowledge

The majority of sensors dedicated to measuring visibility distances (diffusiometer, transmissometer) are expensive to operate and quite often complicated to install correctly. Moreover, this type of equipment cannot easily be placed onboard a vehicle. Use of a camera however does not entail any such obstacles, even though admittedly this topic has only received minimal attention in the literature. Most relevant approaches employ a camera fastened to the road structure, which simplifies the measurement operation given that a reference image is always available. Some methods actually seek to restore the contrast, while others are aimed instead at identifying a contrast threshold within the image.

Given that contrast within the image gets degraded due to atmospheric conditions, Narasimhan and Nayar [6] proposed a method for restoring it. They use, among other tools, Koschmieder's law for modeling the degradation in contrast as a function of distance. They include however two images of the same scene, taken from a fixed camera setup under different meteorological conditions in order to access scene geometry.

Bush and Debes [7] relied upon a fixed camera placed above the roadway for the purpose of measuring visibility

Fig. 1 Placement of the camera within the vehicle

distances. This setup represents, in some respects, a static version of the application we are seeking to develop. Their procedure called for computing contours within the image by virtue of a wavelet transform and then measuring the distance to the furthest pixel that still displays a contrast of greater than 5%, in accordance with CIE recommendations.

Systems that entail use of an onboard camera however are encountered much less frequently. Only Pomerleau [8] actually estimated visibility by means of measuring the contrast attenuation of road markings at various distances in front of a moving vehicle. This approach, based on the "RALPH" system, nonetheless requires the presence and detection of road markings in order to proceed. With the exception of the Pomerleau method, all approaches proposed in the literature make use of a fixed camera, although the military and automobile equipment manufacturers are apparently also conducting research on this topic area (unfortunately, no findings have yet to be published).

## 4 Sensor modeling within the measurement environment

4.1 Presentation of the sensor used

The sensor used in our set-up is a simple black-and-white camera mounted in back of the vehicle windshield, as shown in Fig. 1. Figure 2 sets forth the modeling approach for the sensor within the vehicle environment. In the image reference plane, the position of a pixel is given by its (u,v) coordinates. The coordinates of the optical center projection in the image are designated by (u_0,v_0). θ denotes the angle between the optical axis of the camera and the horizontal, while v_h represents the vertical position of the horizon line. The intrinsic parameters of the camera are its focal length f, and the horizontal size t_{pu} and vertical size t_{pv} of a pixel. We have also made use herein of $\alpha_u = \frac{f}{t_{pu}}$ and $\alpha_v = \frac{f}{t_{pv}}$, and have typically considered: $\alpha_u \approx \alpha_v = \alpha$.

Moreover in this work, we assume that the conversion process between incident energy on the CCD sensor and the gray-level value in the image is linear, which is generally the case for short exposure times. In fact, we use short exposure times (1 to 4 ms) on our onboard camera, so as to reduce the motion blur. Consequently, this assumption can be considered as valid.

4.2 Computation model for the depth at a point seen in the image

Given that just a single camera is being used in this approach, we are unable to gain access to image depth. This problem has been overcome by adopting the hypothesis of a flat road, which makes it possible to associate a distance with each line of the image. In the following discussion, we will present this distance computation model.
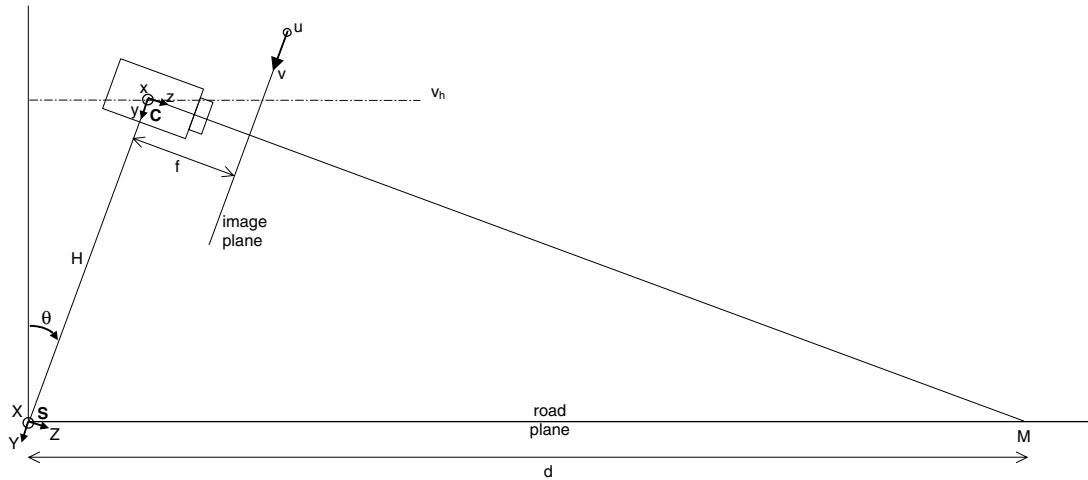
Fig. 2 Modeling of the camera within its environment; it is located at a height of H in the (S, X, Y, Z) coordinate system relative to the scene. Its intrinsic parameters are its focal length f and pixel size t. θ is the angle between the optical axis of the camera and the horizontal. Within the image coordinate system (u, v) designates the position of a pixel (u_0, v_0) the position of the optical center C, and v_h the vertical position of the horizon line
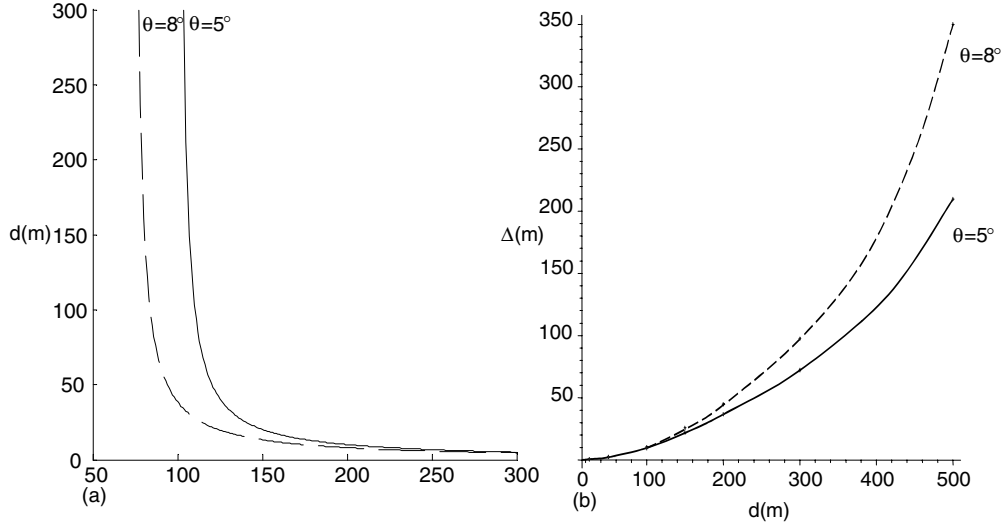
Fig. 3 (**a**) Illustration of the depth computation formula at a point in the image vs. the camera pitch angle. The common parameters used are $H = 2$ m, the ratio of camera focal length to pixel size $\alpha = 500$, and the half-height of the image $v_0 = 144$. The image line number is given horizontally, while distance to the camera in meters is obtained vertically. (**b**) Representation of the distance Δ covered by a pixel at a distance d vs. the camera pitch angle. The common parameters used are the camera height $H = 2$ m, the ratio of camera focal length to pixel size $\alpha = 500$, and the half-height of the image $v_0 = 144$

By applying the pinhole model for the camera, a point with three-dimensional coordinates (x, y, z) within the camera reference system is projected onto the image plane in accordance with the following expression:

$$\begin{cases} u = u_0 + \alpha \dfrac{x}{z} \\ v = v_0 + \alpha \dfrac{y}{z} \end{cases} \tag{4}$$

According to Fig. 2, the horizontal line passing through the optical center makes an angle θ with the z-axis of the camera. Within the image plane, the horizon line can therefore be written as

$$v_h = v_0 - \alpha \tan(\theta) \tag{5}$$

By virtue of Eq. (4), we are able to deduce the following:

$$\frac{v - v_h}{\alpha} = \frac{y}{z} + \tan(\theta) \tag{6}$$

Being positioned within the (S, X, Y, Z) reference corresponding to the scene, Eq. (6) then becomes

$$\frac{v - v_h}{\alpha} = \frac{Y + H}{Z} + \tan(\theta) \tag{7}$$

A point M located on the road at a distance d from the origin S gets parameterized as

$$\begin{pmatrix} X \\ -d\sin(\theta) \\ d\cos(\theta) \end{pmatrix} \tag{8}$$

It can then be deduced that

$$\frac{v - v_h}{\alpha} = \frac{H}{d\cos(\theta)} \tag{9}$$

The distance d can ultimately be expressed by

$$d = \begin{cases} \dfrac{\lambda}{(v - v_h)} & \text{if } v > v_h \\ \infty & \text{if } v \leq v_h \end{cases} \quad \text{where} \quad \lambda = \frac{H\alpha}{\cos(\theta)} \tag{10}$$

Figure 3a displays the distance d calculated using Eq. (10) as a function of the image line number for two distinct camera pitch angles. Since the formula is a hyperbola, the level of inaccuracy or, more precisely, the surface area covered by a pixel increases with the distance. Consequently, the distance estimation will be less accurate and stable for large distances than for small ones. The following section will discuss this aspect in greater detail.

4.3 Estimation of distance computation accuracy vs. camera pitch angle

Thanks to Eqs. (5) and (10) above, we are able to compute the surface area covered by a pixel at the distance d as a function of the camera pitch angle using

$$\Delta(\theta, d) = \frac{\lambda}{\left(\lfloor v_h + \frac{\lambda}{d} \rfloor - v_h\right)} - \frac{\lambda}{\left(\lceil v_h + \frac{\lambda}{d} \rceil - v_h\right)} \tag{11}$$

In this formula, $\lfloor x \rfloor$ designates the whole part of x and $\lceil x \rceil$ the integer greater than or equal to x. The camera pitch angle is typically $8°$, which allows for an effective compromise in contrast between road and sky. By decreasing this value, the horizon line is raised in the image, which serves both to decrease the surface area covered by a pixel and to raise the level of accuracy for large distances; this latter feature proves beneficial as regards our application. From an examination of Fig. 3b, we may consider that the pitch angle

Fig. 4 Example of the image used for sensor calibration. v_1 and v_2 are the lines representing two objects located at distances d_1 and d_2, respectively

only exerts an influence for distance measurements exceeding 250 m.

4.4 Calibration of the sensor

Using the model presented in Fig. 2, a simple estimation of the value of parameter λ makes it possible to calibrate the sensor. To perform this step, knowing the actual distance $d_1 - d_2$ between two points and their coordinates v_1 and v_2 in the image proves sufficient (see Fig. 4). By virtue of Eq. (10), we are ultimately able to obtain the following:

$$\lambda = \frac{d_1 - d_2}{\left(\frac{1}{v_1 - v_h} - \frac{1}{v_2 - v_h}\right)} \tag{12}$$

---

5 Estimation of Koschmieder's law parameters

In Sect. 2.3 above, we presented Koschmieder's law; this section is devoted to studying the mathematical properties

of this formula as well as deducing the existence of an inflection point capable of being detected on the image and providing a basis for our solution.

Following a variable change from d to v based on Eq. (10), Eq. (1) then becomes

$$L = L_0 - (L_0 - L_f)(1 - e^{-k\frac{\lambda}{v - v_h}}) \tag{13}$$

By taking the derivative of Eq. (13) with respect to v, the following is obtained:

$$\frac{dL}{dv} = \frac{k\lambda(L_0 - L_f)}{(v - v_h)^2}\, e^{-k\frac{\lambda}{v - v_h}} \tag{14}$$

The curves depicting both L and its derivative have been represented on Fig. 5, for various values of the extinction coefficient k. From a qualitative standpoint, as fog density increases, the object tends to get obscured more quickly by the luminance emanating from the sky; moreover, the maximum derivative decreases more significantly and deviates more substantially from the horizon line.

By once again taking the derivative of L with respect to v, we obtain the following:

$$\frac{d^2L}{dv^2} = k A(v)\, e^{-k\frac{\lambda}{v - v_h}}\left(\frac{k\lambda}{v - v_h} - 2\right) \tag{15}$$

where $A(v) = \frac{\lambda(L_0 - L_f)}{(v - v_h)^3}$.

The equation $\frac{d^2L}{dv^2} = 0$ has two solutions. The solution $k = 0$ is of no interest to the present discussion. The only useful solution therefore is given in Eq. (16):

$$k = \frac{2(v_i - v_h)}{\lambda} = \frac{2}{d_i} \tag{16}$$

where v_i denotes the position of the inflection point and d_i its distance to the camera. In this manner, the parameter k of Koschmieder's law is obtained once v_i is known.

Moreover, Eq. (16) displays the remarkable property $\lim_{v_i \to v_h} k = 0$, which can serve to detect the presence of
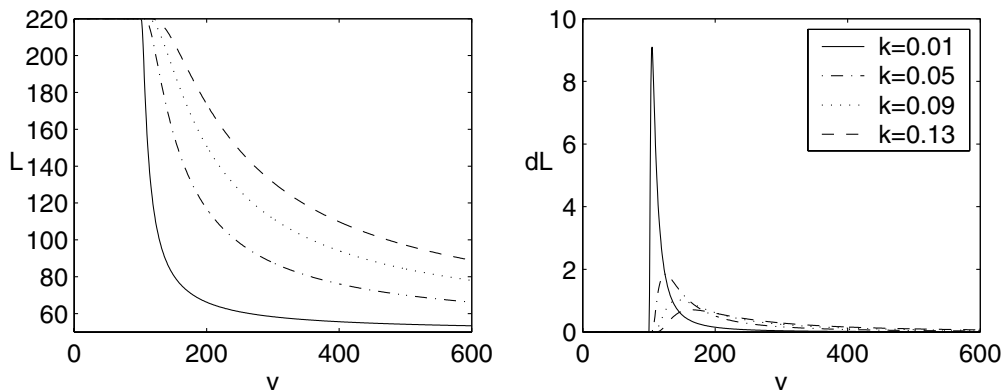
Fig. 5 Various curves representative of Koschmieder's law and of its derivative (level of gray vs. image line number). The common parameters used are $\lambda = 1,000$, $v_h = 100$, $L_o = 50$, $L_f = 220$

fog. If v_i is greater than v_h, fog will indeed be detected; otherwise, it can be deemed that no fog is present.

By virtue of both Eqs. (3) and (16), we are able to deduce the visibility distance V:

$$V = \frac{3\lambda}{2(v_i - v_h)} \tag{17}$$

Let v_v designate the image line representative of the visibility distance. From Eq. (10), we have

$$V = \frac{\lambda}{v_v - v_h} \tag{18}$$

Finally, from Eqs. (17) and (18), we deduce

$$v_v = \frac{2v_i + v_h}{3} \tag{19}$$

Thus, by finding out the inflection point using second derivative of L, we know how to determine precisely the parameter k, which is the crucial point of our method. We must now have to determine precisely the position of this inflection point. This leads to the region growing algorithm presented in the next section.

Furthermore, based on the v_i and v_h values, we are able to deduce the other parameter values of Koschmieder's law through use of L_i and $\frac{dL}{dv}_{|v=v_i}$, which are respectively the values of the function L and its derivative's at $v = v_i$:

$$L_0 = L_i - \frac{(v_i - v_h)^2}{k\lambda e^{-kd_i}} \frac{dL}{dv}_{|v=v_i} (1 - e^{-kd_i}) \tag{20}$$

$$L_f = L_i + \frac{(v_i - v_h)^2}{k\lambda} \frac{dL}{dv}_{|v=v_i} \tag{21}$$

6 Method implementation

In this section, we will demonstrate how to measure in practice the extinction coefficient of fog k. We will start by defining a target region within the image. Afterwards, we will establish a measurement bandwidth on this region before deducing Koschmieder's law parameters and providing a confidence assessment on this measurement.

6.1 Definition of the target region

As shown in Sect. 5, in order to estimate the "meteorological visibility distance," we are required to measure the vertical positions of both the inflection point and the horizon line. As part of an initial approach, the horizon line position can be obtained by searching the focus point in the image of road markings, sidewalks, etc. Such an installation has been proposed in [9].

In order to estimate the position of the inflection point, the problem becomes one of knowing on which object the luminance variation is to be measured. Within our specific context, the most suitable object would be the road as it offers a dark object that always remains present in the scene and acts as an interface between the road and the sky. It also happens to be extensive enough for perceiving a spatial variation in luminance.

In order to ensure coherence with Koschmieder's model, which presupposes an intrinsic luminance L_o, we have assumed that the road is homogeneous and its luminance solely affected by the phenomenon of atmospheric haze. Our algorithm will consequently seek a surface area within the image that exhibits a small continuous variation ingradient when moving line by line. Since the road eventually blends in with the fog, this surface area also includes the sky, with a luminance at infinity of L_f. To segment the road and the sky, we use a fast region growing algorithm which is particularly dedicated to our application. Classical curve evolution based on level-set methods could also be used but would not be fast enough for real time.

6.2 Luminance discontinuities

We begin by extracting the image contours so as to highlight the major contrast breaks constituting the roadway edges, vehicles ahead or crossing, trees, etc. This extraction step is performed by means of a Canny–Deriche filter [10]. We denote by E the set of all relevant contours.

In order to select contours, we apply thresholding with hysteresis (see Fig. 6). t_H and t_L represent the upper and lower thresholds of this process, respectively; both t_L and t_H are set at relatively high values to exclude noise during contour detection and thereby avoid obtaining an interruption at the level of the horizon line.

Neither t_L nor t_H can be constant since their respective values depend directly on the visibility level in the image. Chance would have it that contour detection is slightly sensitive to threshold values, as shown in Fig. 7.

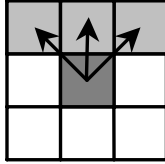### 6.3 Principle behind the region growing algorithm

The next step consists of performing a region growing. In this section, we will define the step's objective and origins as well as its fundamental parameters.
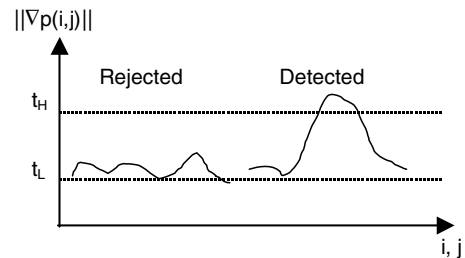
Fig. 6 Principle behind thresholding by hysteresis: points (i, j) are marked by two thresholds. The lower threshold t_L generates the "candidate" points yet remains extremely sensitive to noise. The upper threshold t_H provides a good indication of the existence of a contour
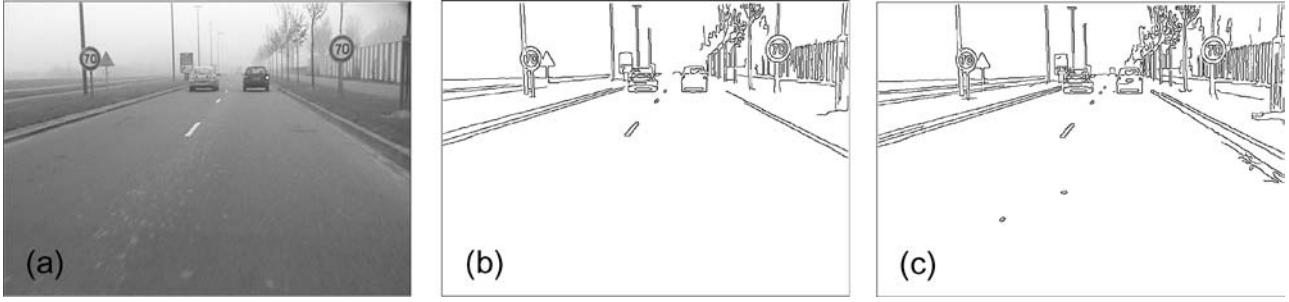
Fig. 7 Sensitivity of the Canny–Deriche filter to threshold values: (**a**) Original image, (**b**) $t_L = 12$ and $t_H = 30$; and (**c**) $t_L = 6$ and $t_H = 20$

Fig. 8 Principle behind region growing. Only the clear gray pixels can be aggregated to the dark gray pixel. The other pixels in the vicinity are ignored

The objective of the algorithm is to identify a region within the image that displays minimal line-to-line gradient variation when crossed from bottom to top, in a configuration that allows for compatibility with Koschmieder's law. From this perspective, the seeds of region expansion are chosen as the pixels of a line from the bottom of the image whose gray level lies close to the median of gray levels for this line. Given the position and optical characteristics of the camera, the majority of pixels in this line represent in fact the road surfacing layer. As such, just the road pixels have been taken into account, as indicated in Fig. 11, thus avoiding for example the increase in certain seeds on a road marking. Similarly, only the three pixels lying above the current pixel (see Fig. 8) can be incorporated into region R. This technique makes it possible to circumvent those objects not to be included within the target region.

The gradient threshold applicable for moving from one line to another on the image still needs to be defined. Based on the discussion in Sect. 5, the maximum vertical gradient G_{max} existing between two successive lines of the image can effectively be deduced. From a purely theoretical standpoint, in the absence of atmospheric diffusion, G_{max} is equal to $L_f - L_o$ at the level of the inflection point. This value unfortunately lacks sufficient constraint to enable expanding the region. We have thus elected to limit the value of G_{max} to t_L. By setting a threshold at this level, the allowable gradient jump between two successive lines is held to a value less than that set forth in Koschmieder's law. Region expansion therefore is compatible with Koschmieder's law, yet by proceeding in this manner, the fog corresponding to a visibility distance of more than 400 m is not detectable. This limitation, however, presents no problem for the target applications herein for the two following reasons:

- Over spans of such length, any estimation of distance proves highly inaccurate in any event (see Sect. 4.3);

- [–] lhe fog density is so weak that it creates no disturbance to either the driver or the measurement instrumentation.

We have opted, once again in order to incite vertical movement at the time of expansion, to apply more highly constraining thresholds in the angled directions rather than in the vertical direction. We thus introduce the notation G^i_{max} where $i \in \{-1, 0, 1\}$ (see Fig. 10), which features the following constraints:

$$G^{-1}_{max} = G^1_{max} < G^0_{max} \leq t_L \tag{22}$$

Typical values of these thresholds lie in the range of 4–8.

6.4 Conditions for pixel aggregation to the target region

In this section, we will establish the four conditions for aggregating a pixel $P(i, j)$ to the target region R. These conditions will be presented in their order of implementation, which coincides with the order of increasing computation time. This approach makes it possible to avoid testing conditions that require the most computation time should the first conditions already prove grounds for rejection.

Pixel $P(i, j)$ is aggregated to the region R, during its composition, provided four conditions have been fulfilled:

- First condition: The pixel does not belong to the region R.

$$P(i, j) \notin R \tag{23}$$

- Second condition: The pixel is not included within a contour detected by means of the Canny–Deriche filter.

$$P(i, j) \notin E \tag{24}$$

- Third condition: The pixel exhibits a certain similarity to the seed P_g. This similarity is evaluated by computing the difference Eq. (25) in level of gray between the investigated pixel and pixel P_g.

$$P(i, j) - P_g \leq \rho n_r \min_{k \in \{-1,0,1\}} G^k_{max} \tag{25}$$

where $\rho < 1$ and n_r designates the line number between $P(i, j)$ and P_g.
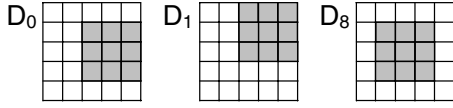
Fig. 9 Zones of the modified Nagao filter. D_2, D_4 and D_6 are deduced from D_0 by means of a 90° rotation. D_3, D_5 and D_7 are deduced from D_1 in the same manner

This condition serves as a safeguard to region expansion, by avoiding the aggregation of pixels that stray too far from the seed for the given line. Without this condition and should a vertical gradient tolerance be set equal to eight, black and white pixels could then be aggregated in fewer than 32 iterations.

– Fourth condition: The pixel is similar to the one located just below. In this context, the similarity will be evaluated through use of a filter inspired by the work of Nagao [11]. Such a filter computes both the average and dispersion for nine different masks and yields the average for the mask featuring the smallest level of dispersion. In our particular case, the result would be the median (see Eq. (28)) of the mask displaying the smallest (see Eq. (27)) spread in levels of gray (see Eq. (26)), so as to enhance noise robustness and computation speed [12]. We have also decided to standardize the shape of masks by introducing square masks [12]. This strategy enables reusing previous computations when expansion extends to the next line, which was not possible with Nagao's original masks.

D_k indicates one of the nine zones shown in Fig. 9. The range of a mask is defined as the difference in level of gray between the clearest and darkest pixels:

$$\text{ext}(D_k) = \max_{(m,n)\in D_k} P(m,n) - \min_{(m,n)\in D_k} P(m,n) \quad (26)$$

We will denote $\widetilde{D_k}$ as the mask displaying the smallest range:

$$\text{ext}(\widetilde{D_k}) = \min_{k\in\{0,8\}} \text{ext}(D_k) \quad (27)$$

Moreover, we can now compute $\tilde{P}(i,j)$, the median level of gray of mask $\widetilde{D_k}$:

$$\tilde{P}(i,j) = \text{median}\{P \in \widetilde{D_k}(P(i,j))\} \quad (28)$$

Using these different notations, the fourth condition, as diagrammed in Fig. 10, can be expressed as follows:

$$\exists \hat{i} \in \{i-1, i, i+1\} / \tilde{P}(i,j) - \tilde{P}(\hat{i}, j-1) < G_{\max}^{i-\hat{i}} \quad (29)$$

As a consequence of the thresholds chosen for the Canny–Deriche filter, the fourth condition implies the second, although the second proves much faster to test and thus serves to reduce the number of candidate pixels for the third and fourth conditions.
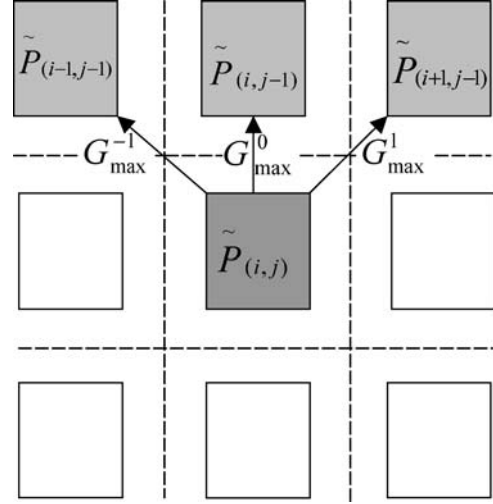
Fig. 10 Diagram representative of the fourth condition of aggregation to the target region for a pixel $P(i,j)$ in its 8-zone

Figure 11 presents various results from region expansion procedures for different values of $G_{\max}$. To the extent possible, region expansion continues until the top of the image has been reached. Even though we did not explicitly intend to focus on the road as well as the sky, it turns out that the region detected by this algorithm contains a portion of both these elements, as Fig. 15b also depicts.

6.5 Composition of a measurement bandwidth

– If the region R does not cross the image from bottom to top, the algorithm is not able to adequately measure luminance variation, in which case no value is the output. This shortcoming may be due to the presence of an obstacle in front of the camera, a large billboard, an excessive drop in luminance at the level of the horizon, or even a bridge extending over the roadway, etc.
– If the region R does cross the image from bottom to top, both the measurement of luminance variation and the computation of Koschmieder's law parameters are possible. Nonetheless, in order to ensure excluding measurements of low-contrast objects located on the edge of the target region, our luminance variation measurement does not span the entire surface area of R.

We will measure luminance variation over a vertical bandwidth B with a maximum width l. From a qualitative standpoint, we are seeking the best vertical path for crossing region R from bottom to top; such a path comprises the set of pixels derived in Eq. (31).
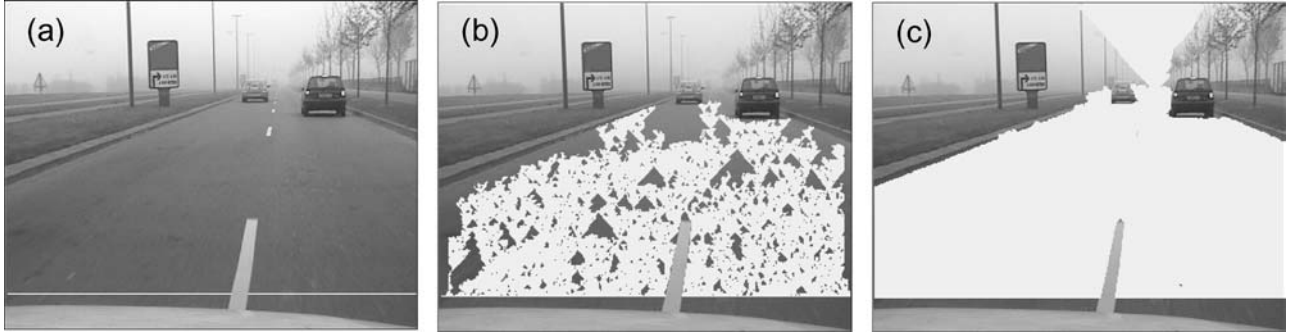
Let us start by providing the definition of a horizontal segment $S_j[i_1, i_2]$ belonging to R:

$$S_j[i_1, i_2] = \{P(i,j) \,|\, \forall i, i_1 \le i < i_2, P(i,j) \in R\} \quad (30)$$

For each line j of R, we then compute the center i_j of the longest horizontal segment belonging to R:

$$i_j = (i \,|\, S_{ij}^+ = S_{ij}^-) \quad (31)$$

Fig. 11 Various results from the region growing as a function of parameter set values $\{G_{max}^{-1} \ G_{max}^{0} \ G_{max}^{1}\}$: (**a**) expansion seeds, (**b**) {1 2 1} (**c**) {5 8 5}

where segments S_{ij}^{-} and S_{ij}^{+} are defined by Eqs. (32) and (33) below:

$$\text{card } S_{ij}^{-} = \max_{i-\frac{l}{2} \leq i_1 < i} \text{card } S_j[i_1, i] \tag{32}$$

$$\text{card } S_{ij}^{+} = \max_{i < i_2 \leq i+\frac{l}{2}} \text{card } S_j[i, i_2] \tag{33}$$

The set of pixels $P(i_j, j)$ constitutes the central axis of B and is ultimately obtained by following the model presented in Eq. (34). This measurement bandwidth search process has been diagrammed in Fig. 12.

$$B = \{S_{i_j, j}^{+}, j = n_1, n_2\} \cup \{S_{i_j, j}^{-}, j = n_1, n_2\} \tag{34}$$

where n_1 and n_2 are the line numbers of the bottom and top of R, respectively.

6.6 Composition of a confidence indicator

This section will be devoted to establishing a confidence indicator C for the measurement of vertical luminance variation on the image. In the ideal case where the fog is very thick and no object is masking the road, the measurement bandwidth is a rectangle whose vertical axis has been centered at i_0, i.e. the B axis for the first line of the image. The shape of the measurement bandwidth is disturbed primarily by the objects it has to avoid incorporating. Consequently, at the level of the objects being circumvented, its axis is offset with respect to i_0 and its width perhaps reduced as well. The confidence C is thus correlated with both the surface area of the measurement bandwidth and the offset of its vertical axis; this correlation is reflected by the following:

$$C = \frac{1}{n} \sum_j \left(1 - \frac{1}{2} \left[\left| 1 - \frac{\text{card } S_{i_j j}^{-} + \text{card } S_{i_j j}^{+}}{l} \right| + \left| \frac{i_0 - i_j}{i_0} \right| \right] \right) \tag{35}$$
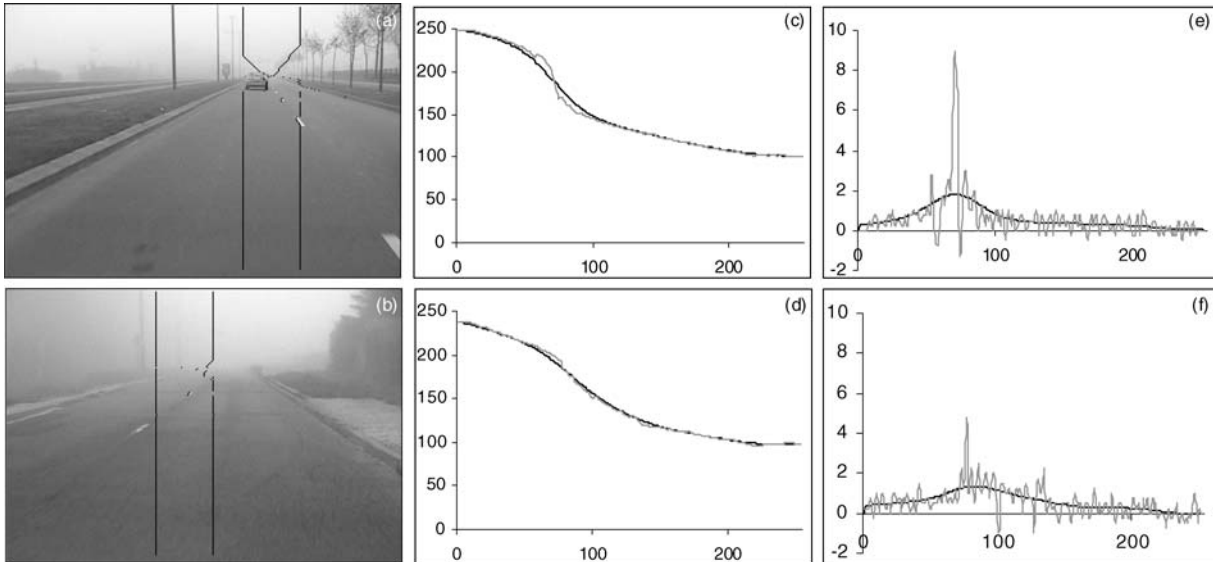
Fig. 12 Examples of measurement bandwidth computations (black lines) under foggy conditions: (**a**) low fog density, and (**b**) high density. Curves representative of the measurement of vertical luminance variation in the image under foggy conditions: (**c**) low fog density, and (**d**) high density. (**e**) and (**f**) depict the derivatives of these curves (gray—without smoothing; black—with smoothing)
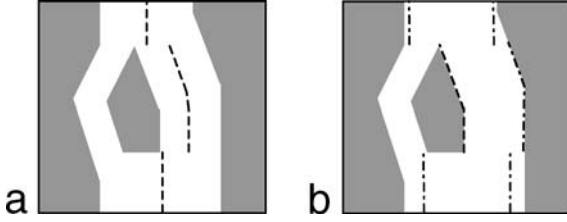
Fig. 13 Diagrammatic example of target region processing (represented in white): (**a**) Computation of the measurement bandwidth axis (represented by dashed lines), (**b**) position deduced from the edges of the measurement bandwidth (represented by dashes)

where n designates the number of measurement bandwidth lines.

6.7 Estimation of the visibility distance

Once the measurement bandwidth has been founded, the median luminance L_j of each bandwidth line is computed, which serves to derive L (the function representing the vertical variation in luminance over the target region R).

$$L_j = \text{median}\{P(i, j) \in B\} \qquad (36)$$

Next, we perform a smoothing of L such that this function is strictly decreasing in order to avoid the detection of too many local inflection points. The derivative of L then gets calculated. Figure 13 provides some examples of the curves obtained. Then, we extract local maximum positions which are the positions of the inflection points. We compute the different parameters k, L_0, and L_f of Koschmieder's law for each local inflection point. We retain the point which minimizes the squared error between the issued model and the measured curve. This yields the position

of the global inflection point v_i and, by the same occasion, the values of both the extinction coefficient and the visibility distance.

7 Method evaluation

7.1 Test video sequences

This method has been tested on three video sequences, each containing over 150 images. In order to highlight the strengths of our algorithm, each sequence exhibits a distinct type of difficulty. In the first, the instrumented vehicle is following two other cars and passes one of them while staying behind the other, under conditions of low fog density. The difficulty herein is twofold: he fog is not thick, making the measurement sensitive to both camera movements and the horizon line computation; and secondly, following the two other vehicles implies the possibility of inserting the measurement bandwidth in between them.

In the second sequence, the instrumented vehicle crosses two cars in a straight line direction on a road with visibility heavily impaired by very thick fog. The difficulty herein pertains to the vehicle intersection and the road, which contains only a few visual indices due to its state as well as to the fog density.

In the third sequence, the vehicle is placed on a turn in the road under very dense fog conditions. Moreover, the road is lined on each side with raised embankments. In this case, the sky cannot be located within the vehicle axis due to the embankments. The combination of thick fog and the curve in the road results in blurring these two elements, which introduces a source of error.

These three sequences have each been illustrated by an image on top of Fig. 14.
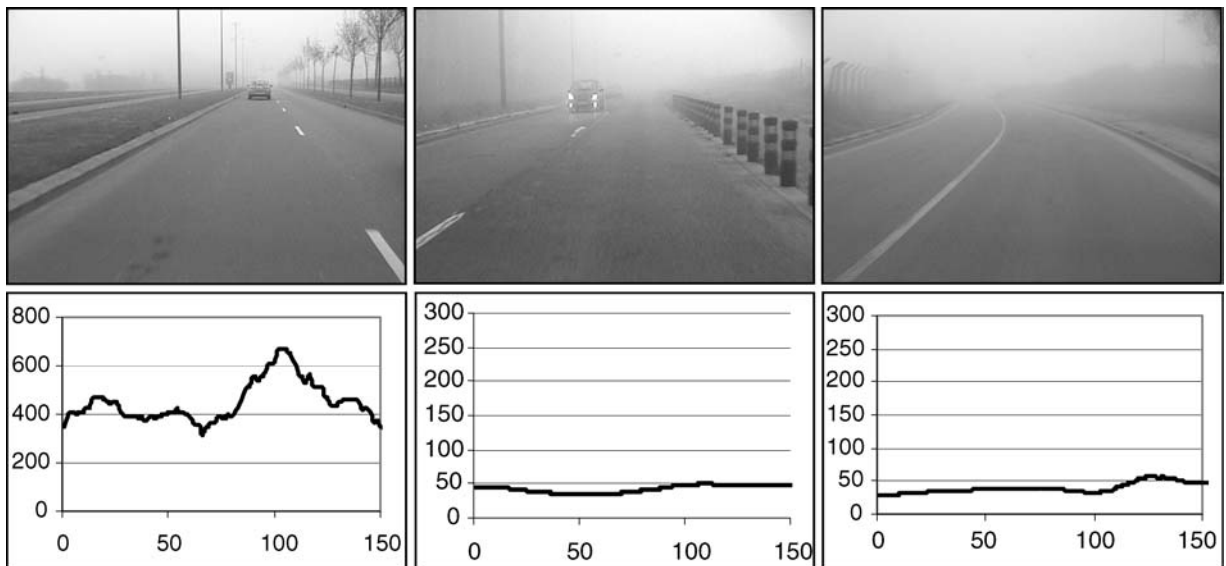
Fig. 14 Visibility distance measurements conducted on the three image sequences (vertical axis: distance, in meters; horizontal axis: image number)
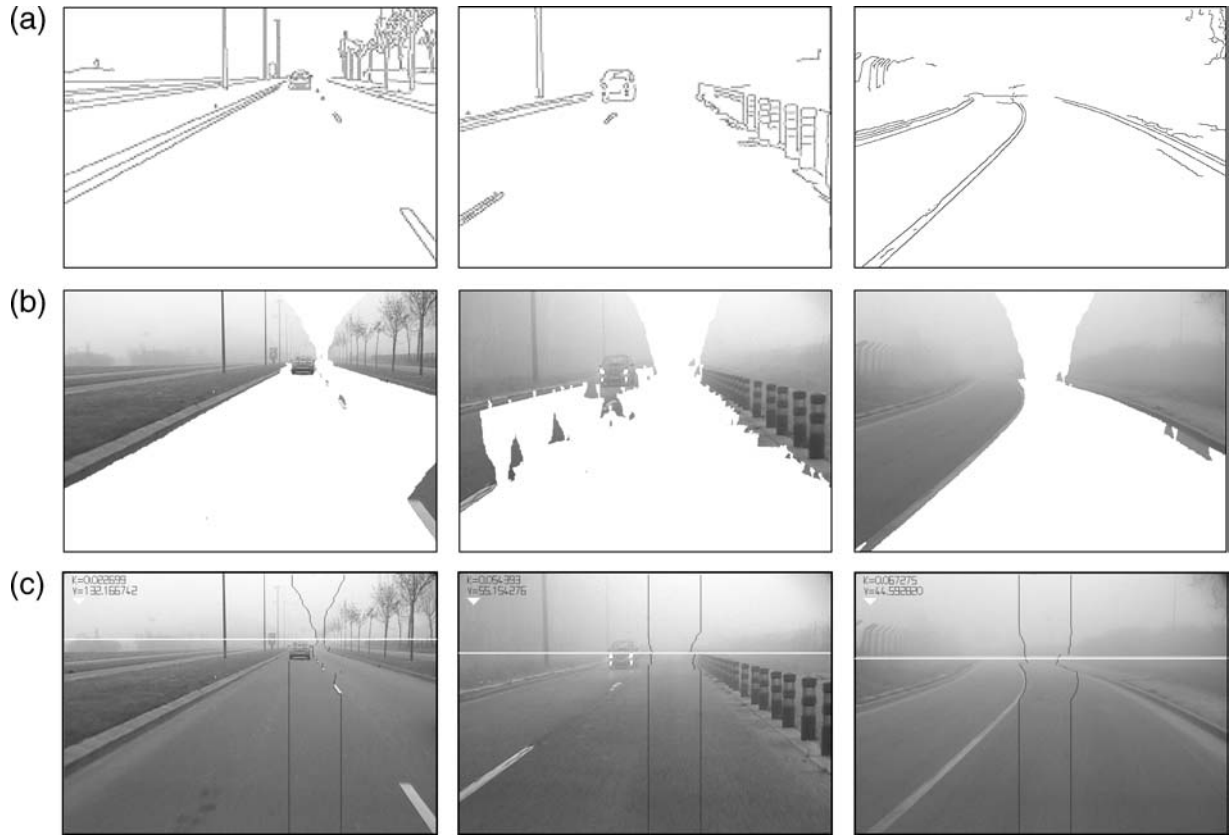
Fig. 15 (**a**) Results of contour detection by means of the Canny–Deriche filter ($\alpha = 1$). (**b**) Region growing results (the target region is painted in white). (**c**) The horizontal white line represents an estimation of visibility distance

7.2 Results

Figure 15a shows the results of the Canny–Deriche filter on three images representative of the sequences detailed in Sect. 7.1. It is obvious that as the fog density increases, the number of contours detected is smaller. On these images, the benefit of thresholding with hysteresis becomes readily apparent. Only very few parasite contours are detected on the roadway. Besides the image to the upper right, the contours are not closed at the horizon level, thereby allowing for region expansion to occur up to the top of the image.

The results of R detection are displayed in Fig. 15b. It is clear that the region expansion algorithm is able to detect neither the road nor the sky in its entirety. It does however detect a large enough zone on the road and sky to allow measuring luminance variation. It should also be noted how the region is capable of making its way in between the vehicles, thus serving to overcome any partial masking of the road.

On some images, region expansion could not be completed due to the presence of a car and a road sign blocking the horizon. As such, region expansion is not carried out since Koschmieder's law hypotheses have not been satisfied; keep in mind that this capability (i.e. to indicate whether or not the region expansion function is operational) constitutes one of the system's key strengths.

Furthermore, Fig. 15c provides the final result of the method. The measurement bandwidth has been implemented so as to allow generating the horizontal white line representative of visibility distance. A triangle in the upper left of each image serves to indicate the state of the system. When white appears, the system is in the operating mode, whereas a black indicator declares the system temporarily inoperative.

Table 1 lists the measurements conducted on the three test sequences. The average and standard deviation of visibility distances (expressed in meters) are accompanied by the extinction coefficient value measured on the 150 images of each sequence. The table also includes the confidence, expressed as a percentage, in the measurement and the percentage of the running time of the algorithm with respect to the duration of the video sequence. Figure 14 shows the

Table 1 Average and standard deviation (shown in parentheses) of Koschmieder law parameters estimated on the three image sequences[a]

Sequence	V (m)	k	$\mathcal{C}$ (%)	RT(%)
1	436 (87)	0.0087 (0.0012)	91 (3)	91.3
2	43 (5.5)	0.07 (0.009)	93 (2)	100
3	40 (7.7)	0.08 (0.013)	88.5 (2)	100

[a]On the last column the percentage of the running time of the algorithm with respect to the duration of the video sequence is shown.

temporal evolution in the visibility distance measurement. In the event of low-density fog, the distance measured is naturally greater. Given the span of a pixel at these distances (see Sect. 4.3), measurements vary rather substantially during the sequence. It may be easily considered however that beyond a measurement of perhaps 250 m, the visibility available for the camera sensor is sufficient and hence the measurement could be clipped at 250 m. On the other hand, under conditions of dense fog (for which this method has been intended), the measurement proves to be very stable.

7.3 Assessment

We have sought to develop herein a stable method. It is real-time performed (smaller than 40 ms for a 360×288 image) on a current-day PC (Pentium 4 running at 2.4 GHz) and runs onboard our prototype vehicle. Then, despite the presence of obstacles (vehicles followed or crossed, turns in the road, etc.), the results are indeed relatively stable and even more so with the increasing fog density. This outcome constitutes one of the method's key advantages.

The problem that must also be faced is to know whether the instabilities are due to local variations in fog density or errors introduced by the method. In the future, to reduce data inaccuracies and make the system more robust, rather than just using one image to determine the fog condition, we could also make use of frame-to-frame coherence in the video sequence.

As a result of the lack of any reference sensor for providing the exact fog density, we have evaluated the accuracy of the method based on a few synthesis imaging samples; this assessment has revealed a high level of accuracy (on the order of 5.5%). In addition, we have built a static test site on test tracks. This site has been equipped with black- and-white reference targets. Using the contrast impairment on these targets, we have computed the meteorological visibility distance. We have obtained a good correlation between the measurements obtained with the reference targets and the presented technique.

8 Conclusion

We have presented herein an original and effective method for measuring the visibility distance using a single camera placed onboard a motor vehicle. Based on a physical diffusion model of the atmosphere, this method enables estimating the "meteorological visibility distance" and merely requires in order to run properly the presence of road and sky, which is verified in each image by use of a region expansion technique. Nonetheless, the technique cannot be employed at night and is inoperable in the event of considerable road masking. For this reason, we are currently developing a new method capable of generalizing our approach.

References

1. Cavallo, V., Colomb, M., Dor, J.: Distance perception of vehicle rear lights in fog. Hum. Factors **43**, 442–451 (2001)
2. Dumont, E., Cavallo, V.: Extended photometric model of fog effects on road vision. Transp. Res. Records: J. Transp. Res. Board (1862), 77–81 (2004)
3. Jaruwatanadilok, S., Ishimaru, A., Kuga, Y.: Optical imaging through clouds and fog. IEEE Trans. Geos. Remote Sens. **41**(8), 1834–1843 (2003)
4. Middleton, W.: Vision Through the Atmosphere. University of Toronto Press, Toronto (1952)
5. International lighting vocabulary. 17.4. Commission Internationale de l'Éclairage (1987)
6. Narasimhan, S.G., Nayar, S.K.: Contrast restoration of weather degraded images. IEEE Trans. Pattern Anal. Mach. Intell. **25**(6), 713–724 (2003)
7. Bush, C., Debes, E.: Wavelet transform for analyzing fog visibility. IEEE Intell. Syst. **13**(6), 66–71 (1998)
8. Pomerleau, D.: Visibility estimation from a moving vehicle using the ralph vision system. IEEE Conf. Intell. Transp. Syst. 906–911 (1997)
9. Tarel, J., Aubert, D., Guichard, F.: Tracking occluded lane-markings for lateral vehicle guidance. IEEE CSCC'99 (1999)
10. Deriche, R.: Using Canny's criteria to derive an optimal edge detector recursively implemented. Int. J. Comput. Vision **2**(1) (1987)
11. Nagao, M., Matsuyama, T.: Edge preserving smoothing. Comput. Graphics Image Process. **9**, 394–407 (1979)
12. Demigny, D., Devars, J., Kessal, L., Quesne, J.: Real time implementation of the nagao image smoothing filter. Trait. Signal **10**(4), 319–330 (1993)
13. Lavenant, J., Tarel, J.-P., Aubert, D.: Procédé de détermination de la distance de visibilité et procédé de détermination de la présence d'un brouillard. French patent 0201822 LCPC / INRETS, (February 2002)

Nicolas Hautière graduated from the École Nationale des Travaux Publics de l'État, France (2002). He received his M.S. and Ph.D. degree in computer vision, respectively, in 2002 and 2005 from Saint-Étienne University (France). From 2002, he is a researcher in the Laboratoire Central des Ponts et Chaussées (LCPC), Paris, France. His research interests include trafic engineering, computer vision, and pattern recognition.

Jean-Philippe Tarel graduated from the École Nationale des Ponts et Chaussées, Paris, France (1991). He received his Ph.D. degree in Applied Mathematics from Paris IX-Dauphine University in 1996 and he was with the Institut National de Recherche en Informatique et Automatique (INRIA) from 1991 to 1996. From 1997 to 1998, he was a

research associate at Brown University, USA. From 1999, he is a researcher in the Laboratoire Central des Ponts et Chaussées (LCPC), Paris, France, and from 2001 to 2003 in the INRIA. His research interests include computer vision, pattern recognition, and shape modeling.

Jean Lavenant graduated from the École Nationale des Travaux Publics de l'État, Lyon, France (2001). He received the M.S. degree in Computer Vision from Jean Monnet university of Saint-Étienne in 2001. In 2001, he was a researcher in the Laboratoire Central des Ponts et Chaussées (LCPC). In 2002, he was a system engineer in Chicago (USA). He is currently an engineer for the french ministry of transports.

Didier Aubert received the M.S. and Ph.D. degree, respectively, in 1985 and 1989 from the National Polytechnical Institut of Grenoble (INPG). From 1989–1990, he worked as a research scientist on the development of an automatic road following system for the NAVLAB at Carnegie Mellon University. From 1990–1994, he worked in the research department of a private company (ITMI). During this period he was the project leader of several projects dealing with computer vision. He is currently a researcher at INRETS since 1995 and works on Road traffic measurements, crowd monitoring, automated highway systems, and driving assistance systems for vehicles. He is an image processing expert for several companies, teaches at Universities (Paris VI, Paris XI, ENPC, ENST) and is at the editorial board of RTS (Research - Transport - Safety).